



Local iron ore identification: comparison to synthesized Fe₃O₄ nanoparticles obtained by ultrasonic assisted reverse co-precipitation method for Auramine O dye adsorption

S. Ben Ayed^a, H.M. Sbihi^b, M. Azam^b, S.I. Al-Resayes^b, M.T. Ayadi^a, F. Ayari^{a,*}

^aLR 05/ES09 Laboratory of Applications of Chemistry to Resources and Natural Substances and to the Environment (LACReSNE), Faculty of Sciences of Bizerte, Carthage University, Zarzouna 7021, Tunisia, emails: fadhilaayari@yahoo.fr (F. Ayari), Sirinebenayed19@gmail.com (S. Ben Ayed), Trabelsiayadi.malika@yahoo.com (M.T. Ayadi)

^bChemistry Department, College of Science, King Saud University, P.O. Box: 2454, Riyadh 1145, Saudi Arabia, emails: adam.sbihi@yahoo.com (H.M. Sbihi), mazamchem@gmail.com (M. Azam), sresayes@ksu.edu.sa (S.I. Al-Resayes)

Received 14 June 2020; Accepted 26 January 2021

ABSTRACT

The synthesis of nanoparticles has to turn out to be a matter of great interest in recent years due to their numerous advantageous properties and applications in several areas. In this study, iron oxide nanoparticles were synthesized via chemical reverse co-precipitation method from ferrous and ferric solutions using ammonium hydroxide as a precipitating agent under ultrasound irradiation. Meanwhile, a natural iron-ore was collected from an iron-ore career situated in the north-west of Tunisia and dried then crushed to minimize particle size. Thus, a comparative study between these iron oxides was carried out based on their physicochemical and optical properties. Therefore, X-ray diffraction, Fourier transform infrared spectroscopy, nitrogen adsorption-desorption isotherms, transmission electron microscopy, and energy-dispersive X-ray microanalysis were used to study physicochemical properties of these materials. UV-vis spectroscopy was used to investigate optical properties. Results show that both materials can be used as heterogeneous catalysts in the Fenton process and that the novel natural iron oxide is better than the synthesized one because of its more developed surface area, its low cost, and its abundance. Eventually, preliminary adsorption studies of Auramine O, as a model of anionic dye, onto these two materials have shown that natural iron oxide is more effective adsorbent than the synthesized nanoparticles with an adsorption rate of 99%. Adsorption process followed Langmuir type and pseudo-second-order kinetic, suggest monolayer adsorption and physisorption process.

Keywords: Reverse co-precipitation; Nanoparticles; Iron oxide; Tunisian iron-ore; Adsorption, Auramine O dye; Modeling

1. Introduction

Water is used in agriculture, construction, chemical industry, and in several other activities of human beings. According to the United Nations, the main priority of poor countries in Africa should be not technological knowledge

or financial support but potable water affordable for the population [1].

Treatment of industrial wastewaters is a long-lasting issue of environmental relevance. Numerous industrial activities and especially chemical ones produce wastewaters containing a vast variety of toxic, persistent, and non-biodegradable organic pollutants. These organic pollutants must

* Corresponding author.

be treated as economically as possible in an environmentally friendly manner. Advanced oxidation processes (AOP) might be considered as rising technologies for the sustainable removal of pollutants from agricultural, urban, and industrial wastewater. They have exhibited great potential for the treatment of industrial wastewaters [2,3]. These simple processes work at near ambient temperatures and pressures implicating the generation of hydroxyl radicals in appropriate quantity to permit oxidizing the organic pollutants.

AOPs have been used for the degradation and mineralization of organic pollutants such as phenolic compounds [4], agrochemicals [5], and pharmaceuticals [6]. The Fenton process is a strong oxidation system amongst AOP and has been successfully applied for the removal of organic contaminants [7]. This process is known as the reaction between iron ions as a catalyst and hydrogen peroxide as an oxidant to generate extremely active species, principally non-selective OH^\bullet radicals with an oxidation potential of 2.8 V. However, this article will focus on the characterization of materials based on iron in order to use them later as catalysts and their application as adsorbents for auramine O dye removal due to their adsorptive properties.

Iron oxides are plentifully available minerals that exist in the earth's crust. Out of the 16 known iron oxides and hydroxides [8], magnetite (Fe_3O_4), goethite (αFeOOH), maghemite ($\delta\text{Fe}_2\text{O}_3$), and hematite ($\alpha\text{Fe}_2\text{O}_3$) have been attractive alternatives for remediation groundwater [9] and wastewater and are broadly used in heterogeneous catalysis processes. Magnetite nanoparticles have applications in several areas, such as tumor and cancer diagnosis and treatment [10], biomedical [11], and as a magnetic resonance imaging (MRI) contrasting agent [12].

The magnetite can be synthesized by various methods, including hydrolysis [13], the sol-gel technique [14], ultrasound irradiation [15], microemulsions [16], thermal decomposition [17], and co-precipitation [18]. Co-precipitation is the most commonly used because of its simplicity and efficiency and provides a spherical shape with particle size below 25 nm [19]. However, magnetite nanoparticles are the most studied materials due to their response to the magnetic field through the superparamagnetic behavior at room temperature with high saturation magnetization. In addition, their textural, non-toxicity, and catalytic properties in different reactions are suitable for catalysis applications as catalysts. On the other hand, the use of the natural heterogeneous catalyst in the Fenton process could be a potential alternative owing to their low cost and abundance. Therefore, locally iron-ore was defined and characterized in this study, which is used for the first time by our laboratory for its catalytic properties to textile wastewater and dyes aqueous solutions treatment, important results were published [20,21].

Different physico-chemical characteristics of these oxides make them more or less appropriate for oxidative reactions. From these features, surface area, pore size/volume, and crystalline structure have principal effects on their activities. Thus, the main objective of this work is to compare physicochemical, structural, and textural properties, as well as optical characteristics of these materials (synthesized iron oxide and natural iron-ore), afterward compare their affinity toward adsorption of anionic dye (Auramine O).

2. Experimental

2.1. Chemicals

Chemical reagents used in this work were ferrous sulfate ($\text{FeSO}_4 \cdot 7\text{H}_2\text{O}$), ferric chloride ($\text{FeCl}_3 \cdot 6\text{H}_2\text{O}$), and ammonium hydroxide (28%). Synthetic wastewater was prepared with distilled water and Auramine O (AO) ($\text{C}_{17}\text{H}_{21}\text{N}_3\text{Cl}$, M.W. = 303, 83 g mol⁻¹, λ_{max} = 432 nm). All chemicals were of analytical grade and were directly used without any further purification.

2.2. Materials

2.2.1. Natural iron oxide

Natural iron-ore used in this work was collected by works staff from iron-ore careers situated in the north-west of Tunisia.

After being collected, the sample was dried and crushed to minimize particle size. Natural material being labeled MF (Fig. 1).

2.2.2. Preparation of magnetic nanoparticles

Magnetite nanoparticles Fe_3O_4 were synthesized by reverse co-precipitation method using ammonia as precipitation agent under ultrasound irradiation [22]. This method is the most efficient and the simplest chemical way to obtain magnetic particles [23]. NH_4OH solution was used in this work as precipitating agent instead of NaOH in order to get magnetite nanoparticles with smaller size and higher crystallinity [24]. In a typical experiment, we mixed 5.0 mL of 1.0 mol L⁻¹ $\text{FeCl}_3 \cdot 6\text{H}_2\text{O}$ solution and 10.0 mL of 0.5 mol L⁻¹ $\text{FeSO}_4 \cdot 7\text{H}_2\text{O}$ solutions and get a solution with orange color (Fig. 2a). The mixture was added dropwise into 20 mL of 3.5 mol L⁻¹ ammonium hydroxide solutions at 60°C under ultrasound irradiation. The reaction



Fig. 1. Photography of natural iron ore sample.

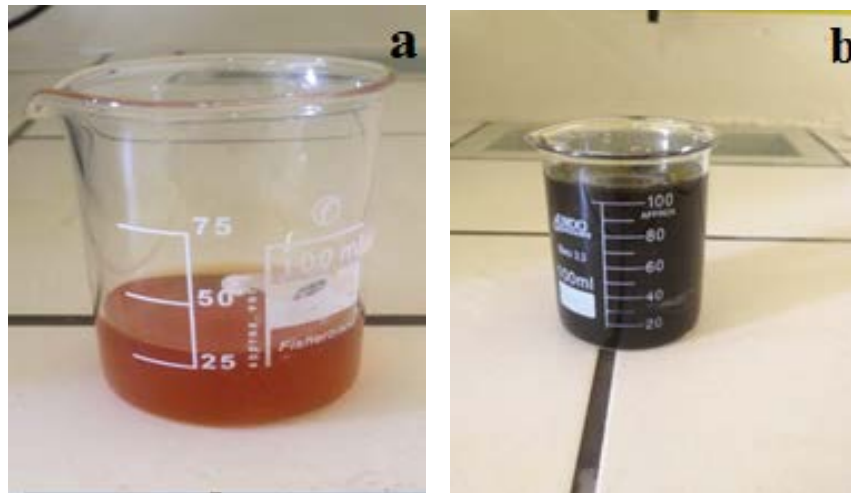
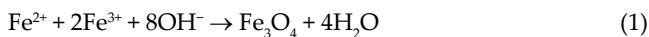


Fig. 2. Preparation of magnetic nanoparticles: (a) solution of Fe^{3+} and Fe^{2+} with 2:1 M ratio and (b) Fe_3O_4 nanoparticles solution.

proceeded for 30 min and the overall reaction of magnetite Fe_3O_4 can be written as [25]:



Synthesized Fe_3O_4 was marked by the appearance of intense black color (Fig. 2b). The product was collected using a magnet, washed several times with distilled water to eliminate chlorine, sulfur, and base excess, next dried in an oven at 90°C for 12 h and kept in a stoppered bottle for later use.

2.3. Characterization of the magnetite nanoparticles and natural iron oxide

Physicochemical characterization was performed using several techniques.

Crystalline forms of the materials were characterized by X-ray diffractometer (XRD) using a PANalytical X'Pert HighScore Plus diffractometer (Malvern, Almelo, The Netherlands), with monochromatic Cu-K radiation source ($\lambda = 1.5418 \text{ \AA}$) generated at 40 kV and 40 mA. The X-ray diffraction (XRD) profiles of the samples were recorded in the angular range of 25° – 70° .

Chemical structures were subjected using Fourier transform infrared (FTIR) model spectrum. Dried samples were ground with potassium bromide (KBr) to produce pellet, which was examined in a wavelength range of 480 – $4,000 \text{ cm}^{-1}$. Textural parameters were studied by means of adsorption–desorption isotherms of N_2 at 77 K by a Quantachrome model Nova 1200e surface and porosity analyzer. Samples were out gassed at 150°C for 12 h in a dynamic vacuum before physisorption measurements. Specific surface area (S_{BET}) values were calculated using Brunauer–Emmet–Teller (BET) method. Morphology and particle size distribution of these samples were determined by transmission electron microscopy (TEM). Images were obtained using TEM machine operated at 200 kV. Elemental composition was estimated by EDX energy dispersive X-ray microanalysis.

Optical properties were determined by UV-vis diffuse reflectance spectroscopy (DRS) using UV-visible spectrophotometer (Shimadzu UV-2700, Kyoto, Japan).

2.4. Adsorption experiments

Adsorption of AO on both materials at different parameters such as initial dye concentration, adsorbent amount, and adsorbant/adsorbate contact time were carried out via batch method using Erlenmeyer flasks under magnetic stirring.

For that, at 50 mL of AO dye solution (5 mg L^{-1} , $\text{pH} = 6.3$), a known dose of adsorbent was added, the mixture was agitated with a constant stirring rate of 100 rpm at room temperature (25°C) until equilibrium was reached, after that, all samples were centrifuged for 30 min and filtered. Residual dye's concentration was determined using UV-vis spectrophotometer (Shimadzu Model Perkin Elmer, Waltham, USA) by the measurement of absorbance at the maximum absorption wavelength of AO ($\lambda_{\text{max}} = 432 \text{ nm}$). The removal percentage of AO ($Y\%$) was calculated using the following equation:

$$Y\% = \frac{C_0 - C_e}{C_0} \times 100 \quad (2)$$

where C_0 and C_e are the initial concentration and equilibrium concentration of AO, respectively.

3. Results and discussion

3.1. Fe_3O_4 nanoparticle characterization

3.1.1. Superparamagnetic properties of Fe_3O_4 nanoparticles

Synthesized magnetic nanoparticles (MNPs) indicate a perfect response to any external magnetic field, so it was easy to separate the liquid and solid phases as shown in Fig. 3.

3.1.2. Phase structure of the synthesized MNP

3.1.2.1. Powder XRD analysis

XRD pattern of MNPs (Fig. 4) shows six major diffraction peaks in the whole spectrum at 2θ values of 30.36° , 35.8° , 43.33° , 53.1° , 57.48° , and 63.09° , which are greatly corresponding to (2 2 0), (3 1 1), (4 0 0), (4 2 2), (5 1 1),

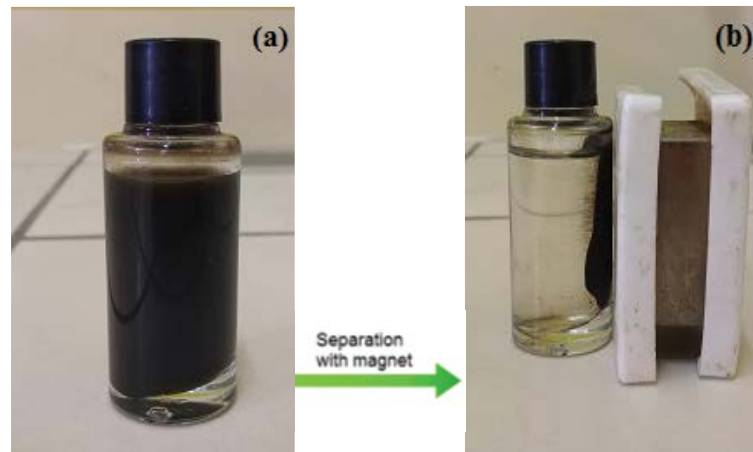


Fig. 3. Superparamagnetic attitudes of the MNPs: (a) Fe_3O_4 -NPs solution and (b) separation of synthesized Fe_3O_4 -NPs from the reaction mixture using an external magnet.

and (4 4 0) planes of the standard XRD data for the cubic Fe_3O_4 phase of the reverse spinel crystal structure (JCPDS file No. 19-0629) [26]. These crystalline entities exhibit the typical pattern of Fe_3O_4 , and the absence of any other phase such as hematite, magnetite, or $\text{Fe}(\text{OH})_3$, which were the habitual co-products in the chemical reverse co-precipitation process. The strong and sharp peaks clearly prove that the attained nanoparticles had a highly pure crystalline nature. Results are in agreement with the XRD standard for the magnetite nanoparticles [27].

Average crystallite size has been carried out from Debye–Scherrer formula (Eq. (3)). This parameter was found to be 16 nm.

$$D = \frac{K\lambda}{\beta \cos \theta} \quad (3)$$

where D is the crystallite size, K is the Debye–Scherrer constant ($K = 0.89$ for magnetite), λ is the wave length of the $\text{Cu-K}\alpha$ irradiation ($\lambda = 0.1541$ nm), β is the full width at half maximum intensity of diffraction peak (FWHM), and θ is the scattering angle (the Bragg angle).

3.1.2.2. FTIR analysis

IR spectra (Fig. 5) show a broad peak at about $3,440 \text{ cm}^{-1}$ relevant to stretching vibrations of $-\text{OH}$ group assigned to OH^- adsorbed by magnetite nanoparticles [28]. The absorption bands checked at $1,640$ and $1,400 \text{ cm}^{-1}$ correspond to stretching vibration of magnetite surface OH -groups [28].

Two significant peaks at about 565 and 440 cm^{-1} attributed to Fe-O vibrations bond. These intrinsic stretching vibration bands correspond, respectively, to the metal (Fe) in tetrahedral and octahedral sites [29]. This result can be assigned to the high crystallinity nature of the Fe_3O_4 nanoparticles and proves the formation of inverse type spinel structure of Fe_3O_4 nanoparticles [8,30]. In general, magnetite crystals are covered by mixed octahedral/tetrahedral and octahedral layers along the {111} direction

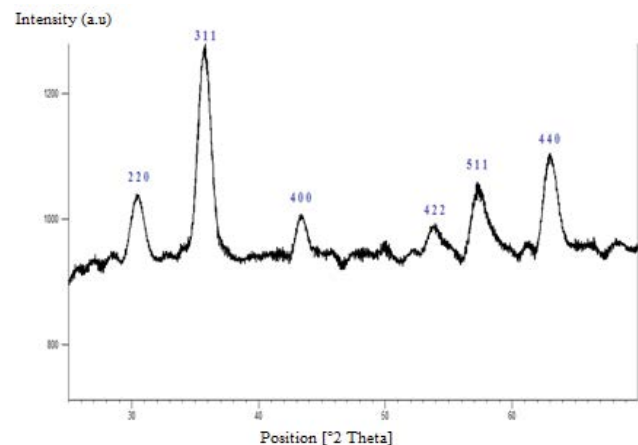


Fig. 4. XRD pattern of the Fe_3O_4 MNPs sample.

(Fig. 6) [8]. The attained results are in good agreement with the XRD analysis.

3.1.2.3. Surface analysis and porosity

Porous properties of iron oxide powder estimated by N_2 adsorption–desorption method (Fig. 7) shows an adsorption isotherm of type IV according to the International Union of Pure and Applied Chemistry classification. The specific surface area (S_{BET}), determined by means of the Brunauer–Emmett–Teller method (BET) was found to be $30.695 \text{ m}^2 \text{ g}^{-1}$. Total pore volume and pore size distribution determined by Barret, Joyner, and Halenda (BJH) method using desorption isotherms indicate that this product is a mesoporous material with different pore sizes of 2.1, 3.6, and 7 nm (Fig. 7 inset) and a total pore volume of $0.0821 \text{ cm}^3 \text{ g}^{-1}$.

3.1.2.4. Transmission electron microscopy

Fe_3O_4 micrograph (Fig. 8) shows that the examined particles are spherical in shape with a narrow size distribution

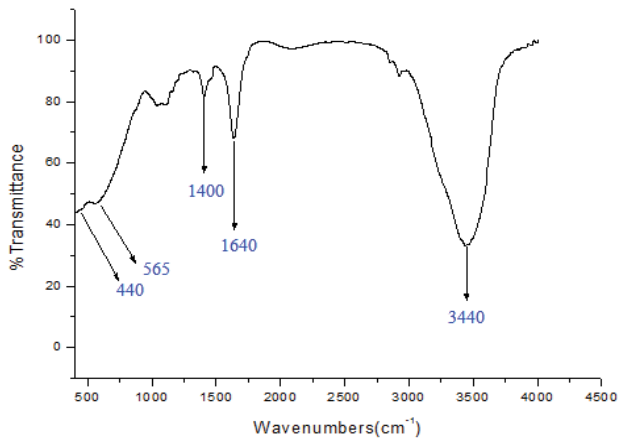


Fig. 5. IR spectra of the magnetite nanoparticles (Fe_3O_4).

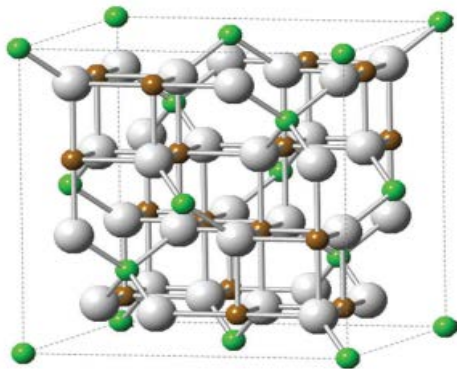


Fig. 6. Crystal structure of Fe_3O_4 , green atoms are Fe^{2+} , brown atoms are Fe^{3+} , and white atoms are oxygen.

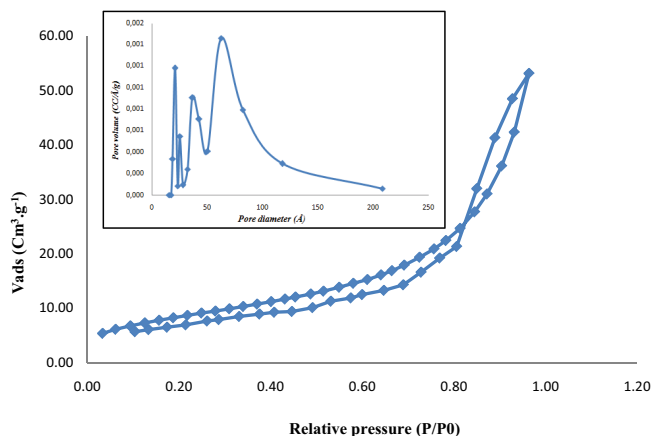


Fig. 7. N_2 adsorption/desorption isotherm at 77 K by Fe_3O_4 nanoparticles.

in the range of 10–27 nm. Moreover, most particles have an average diameter of 15 nm which matches well with the XRD data. It is important also to note that the particles tend to agglomerate.

A selected area electron diffraction pattern (SAED) of the Fe_3O_4 nanoparticles is shown in Fig. 8d. The clear and

well-defined diffraction rings in the SAED pattern indicate that the attained Fe_3O_4 nanoparticles are great crystalline materials and single crystalline in nature. The interplanar spacing (Fig. 8c) is measured to be 0.25 nm, which is in accordance with the (3 1 1) lattice fringes in the inverse spinel Fe_3O_4 nanoparticles [31], and in good agreement with the XRD result.

3.1.2.5. EDX analysis

EDX spectra of Fe_3O_4 nanoparticles (Fig. 9) indicate the presence only of Fe element ($W\% = 97.6$) which suggests that the product is pure. It is important to note that the preparation condition completely promotes the formation of Fe_3O_4 . The small two peaks at 2.30 and 2.70 kV indicate respectively the presence of sulfur and chlorine elements which was used for the synthesis of Fe_3O_4 ; they are considered as impurities that can be eliminated thoroughly by washing the product several times with distilled water.

Carbon and copper peaks were related to the carbon-coated copper grid used when preparing the sample for TEM-EDX analysis for better visibility of the surface morphology.

3.1.2.6. Optical properties by DRS studies

Diffuse reflectance spectra of Fe_3O_4 nanoparticles in the range of 200–1,200 nm (Fig. 10) suggest that this material adsorbs in the ultraviolet and visible region owing to the existence of two adsorption bands at $\lambda = 333$ nm and 746 nm, respectively. This maybe corresponded to its small band gap [32]. This result proves that the optical response of synthesized magnetite particles could be prolonged from the ultraviolet light region to the visible light region which suggests that this product is a photocatalyst. Both of these light energies could be used by Fe_3O_4 for photocatalytic activity.

3.2. Natural iron oxide characterization

3.2.1. XRD analysis

XRD analysis is applied to identify the structure and the mineralogical composition of the studied natural iron oxide (Fig. 11). Results show peaks related to goethite FeOOH [33], hematite Fe_2O_3 [34], and magnetite Fe_3O_4 [35] (Table 1). Furthermore, peaks of quartz (Q) and kaolinite (K).

3.2.2. FTIR analysis

IR spectra of MF (Fig. 12) shows absorption bands at about 890 and 783 cm^{-1} relevant to O–H bending bands in goethite (Fe-OH) corresponding to the vibrations in and out of the plane respectively [36].

Peaks at 479 and 560 cm^{-1} are, respectively, attributed to the symmetric stretching vibration bands of Si–O and O–Fe–O functional groups [36,37]. Bands at 1,041 and 1,642 cm^{-1} are assigned, respectively, to asymmetric stretching vibration of Fe–O–Si and O–H. The band expounded at 1,451 cm^{-1} is related with the asymmetric stretching vibration of C=O. Eventually, the band at 3,388 cm^{-1} is

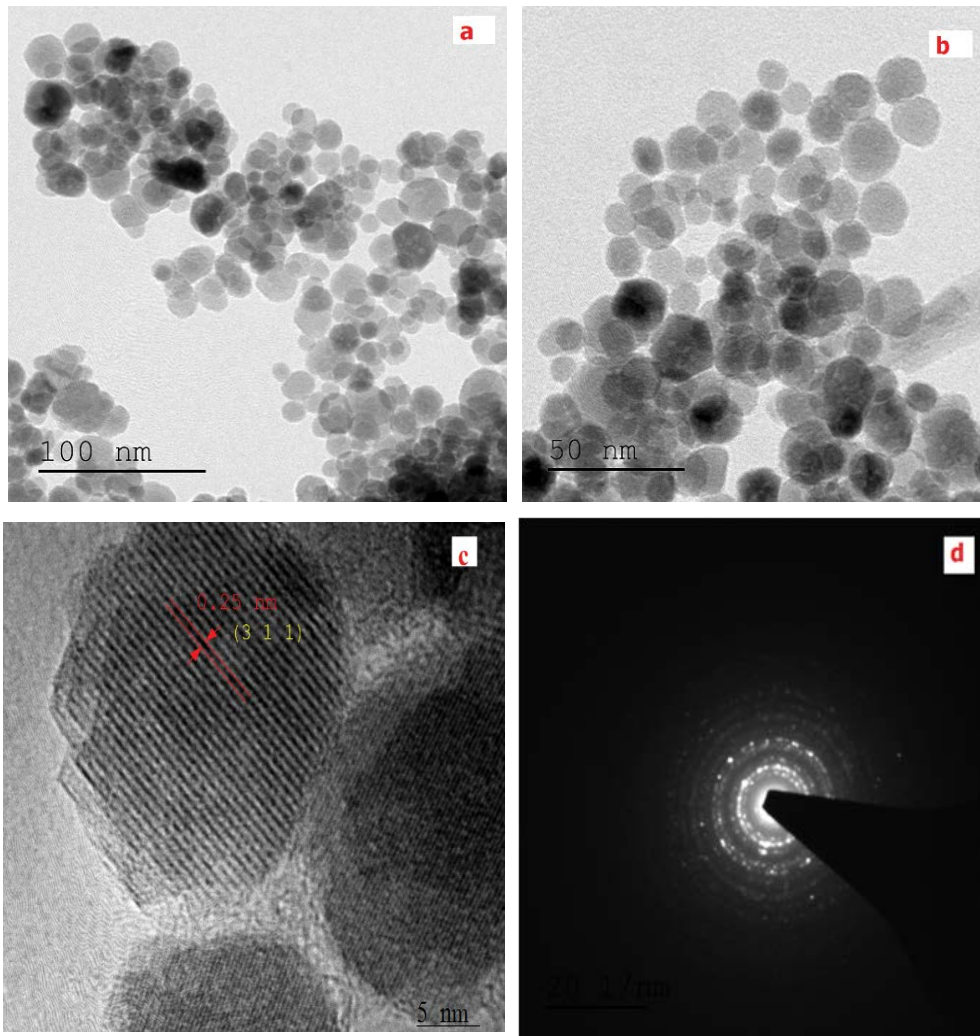


Fig. 8. TEM micrographs of Fe_3O_4 at different scale: 100 nm (a), 50 nm (b), and 5 nm (c) and the associated selected area diffraction (SAED) pattern for the powder (d).

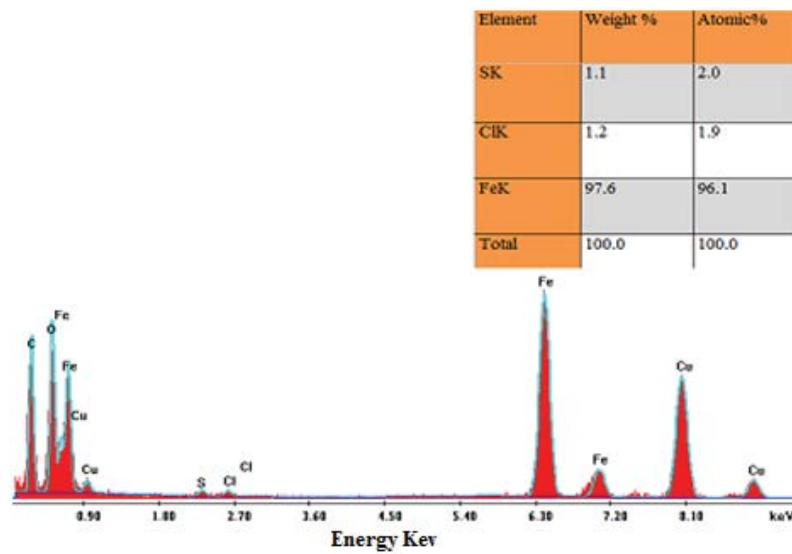


Fig. 9. EDX spectrum of Fe_3O_4 .

related to the hydrogen-bonded hydroxyl groups stretching vibration [20].

3.2.3. Surface analysis and porosity

MF BET analysis (Fig. 13a) shows that N₂ adsorption isotherm is of type IV with hysteresis loop according to IUPAC classification [38]. S_{BET} specific surface area of MF powder was determined to be 45.868 m² g⁻¹. Total pore volume and pore size distribution were determined by Barret, Joyner, and Halenda (BJH) method using desorption isotherms. The result reveals that MF powder has a total pore volume of 0.10 cm³ g⁻¹. The pore size distribution is displayed in Fig. 13b, indicating that the product is a microporous material with a pore size of about 2 nm which is different from the synthesized iron oxide material (mesoporous).

Compared to the synthesized iron oxide nanoparticles results (Table 2), the natural iron oxide has approximately the same total pore volume value but a much higher BET specific surface area and very lower pores size.

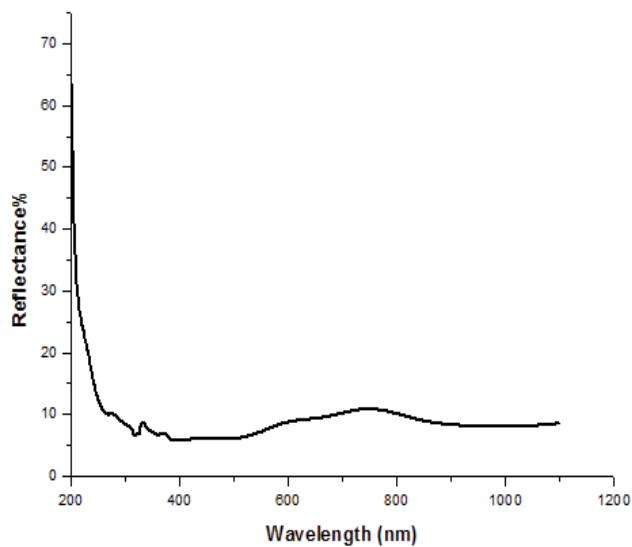


Fig. 10. UV-visible diffuse reflectance spectra (DRS) of Fe₃O₄ nanoparticles.

3.2.4. TEM-EDX

Morphological structure of MF gives by microscope analysis through TEM instrument (Fig. 14) seems different from synthesized Fe₃O₄ nanoparticles, MF sample present a rod shape with different lengths and thickness. It is worth noting that the iron ore sample was diluted in ethanol and subjected to ultrasound for 10 min and then a small drop of the suspension was placed on a thin carbon film on a TEM copper grid, letting it dry, and coated with a thin carbon layer to enhance stability under the beam.

The EDX analysis (Fig. 14c) reveals the presence of different elements: Fe, Si, Al, As, and Mg with a weight percent of 63.6, 30.2, 3.2, 1.7, and 1.3, respectively.

3.2.5. Optical properties

UV-vis diffuse reflectance spectra of natural iron oxide (Fig. 15) show two adsorption bands at the visible light region at λ = 611 and 749 nm suggested that the

Table 1
Identification of natural iron ore by XRD

| Phase | 2θ (°) | d _{hkl} (Å) |
|-----------|--------|----------------------|
| Goethite | 15.08 | 5.89 |
| | 24.38 | 3.64 |
| | 34.76 | 2.57 |
| | 35.70 | 2.51 |
| | 41.36 | 2.24 |
| | 50.16 | 1.81 |
| | 53.36 | 1.71 |
| Hematite | 59.18 | 1.56 |
| | 33.35 | 2.08 |
| | 40.18 | 2.24 |
| | 64.053 | 1.45 |
| Magnetite | 21.37 | 4.16 |
| | 29.97 | 3.07 |
| | 36.7 | 2.43 |
| | 61.35 | 1.50 |
| | | |

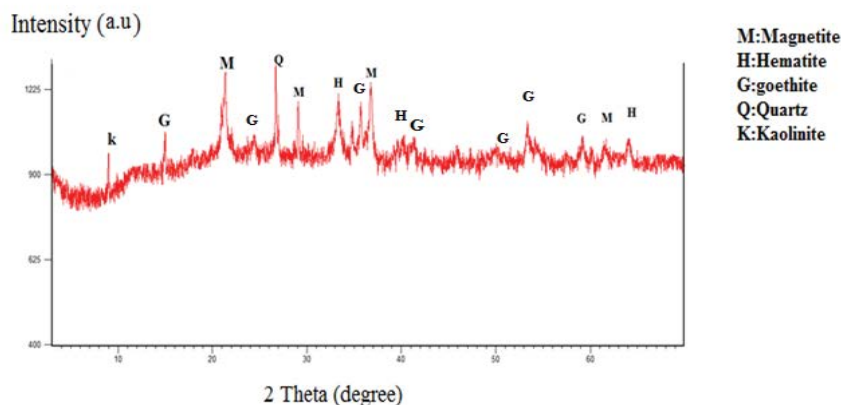


Fig. 11. Powder XRD pattern of the natural iron oxide sample.

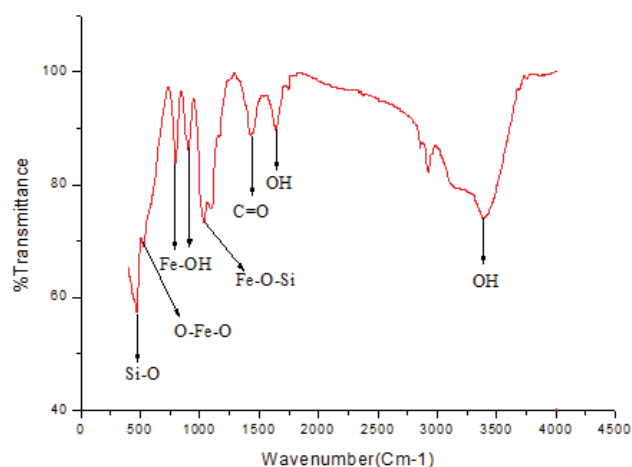


Fig. 12. IR spectra of natural iron oxide.

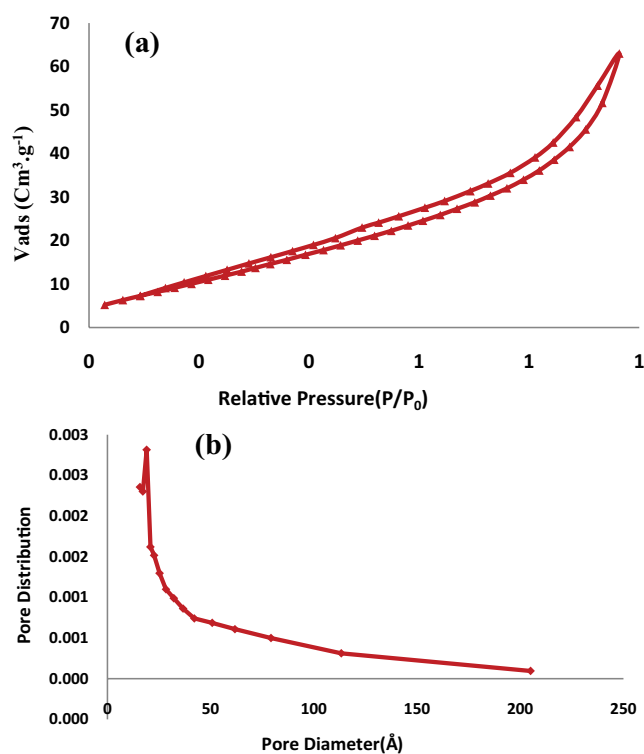


Fig. 13. Nitrogen adsorption/desorption isotherms at 77 K for iron-ore (a) and BJH-method pore size distribution curves from nitrogen sorption data (b).

optical response of MF could be prolonged to the visible light region. Only visible light energy could be used by MF for realizing the photocatalytic activity.

3.3. Adsorption performance

3.3.1. Effect of adsorbent type

In order to compare the adsorption performance of these materials for AO dye removal from aqueous solution;

Table 2

Textural properties of the studied samples: magnetite and MF

| Samples | Magnetite | MF |
|---|-----------|--------|
| S_{BET} ($\text{m}^2 \text{g}^{-1}$) | 30.695 | 45.868 |
| $S_{\text{BJH/mesp}}$ ($\text{m}^2 \text{g}^{-1}$) | 25.949 | 44.170 |
| $V_{\text{BJH/mesp}}$ ($\text{cm}^3 \text{g}^{-1}$) | 0.0821 | 0.092 |
| V_{ads} ($\text{cm}^3 \text{g}^{-1}$) | 0.08 | 0.10 |
| D (\AA) | 62.462 | 18.99 |

S_{BET} : BET surface area, $S_{\text{BJH/mesp}}$: mesopore surface area, $V_{\text{BJH/mesp}}$: mesopore volume, V_{ads} : volume of N_2 adsorbed at $P/P_0 = 0.98$, D : average pore diameter.

0.2 g of each adsorbent was added to 50 mL of dye solution (5 mg L^{-1}) for an adsorbent/adsorbate contact time interval varying from 20 to 180 min. Experiments are carried out at room temperature (25°C).

Results (Fig. 16a) reveal that adsorption equilibrium is reached after 75 min for both materials and that natural iron oxide (MF) is a more efficient adsorbent than Fe_3O_4 nanoparticles with 69% AO dye removal. This result can be explained by the MF structural and textural properties; in fact, MF has an important specific surface, so more active sites for dye retention.

Thus, we will only focus on studying the removal of AO dye by the natural iron oxide.

3.3.2. Preliminary study of AO dye adsorption onto MF

3.3.2.1. Effect of adsorbent dose

Effect of iron ore dose on AO dye adsorption has been studied. Experiences were carried out at room temperature with an initial dye concentration of 5 mg L^{-1} , a contact time adsorbate/adsorbent of 75 min, and different adsorbent amount variants from 0.2 to 1.6 g. Results (Fig. 16b) show that the removal efficiency increases gradually with the adsorbent dose to reach saturation at about 98% of dye removal with 1.2 g of MF amount. This is due to the increase in the number of active sites. So, 1.2 g of MF will be used as an optimal dose in the following experiments.

3.3.2.2. Effect of initial dye concentration

A series of dye solutions, at different concentrations varying from 5 to 50 mg L^{-1} were prepared, to each solution 1.2 g of MF was added then the mixture was stirred for 75 min. Experiments were carried out at room temperature. The mixtures were then centrifuged; the supernatant of each solution was analyzed by a UV-visible spectrophotometer at the appropriate wavelength.

As it can be seen from Fig. 16c, removal of AO decreases from 98% to 51% when the initial dye concentration increases gradually from 5 to 50 mg L^{-1} . This can be attributed to the saturation of active sites on the adsorbent surface by AO molecules. Thus, some of the AO dye molecules were left in the aqueous solution. So, increasing the initial dye concentration inhibits the adsorption process.

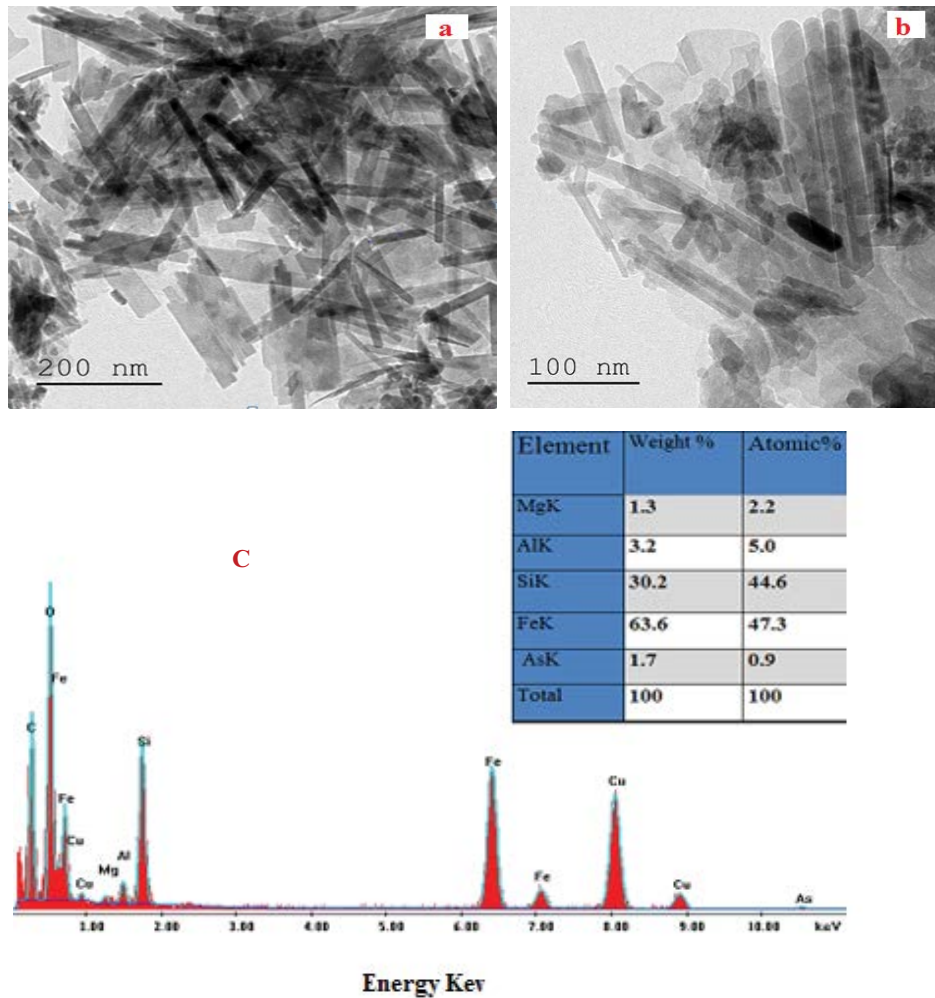


Fig. 14. TEM micrographs of natural iron oxide at different scales: 200 nm (a), 100 nm (b), and (c) EDX spectrum of natural iron oxide.

Optimum conditions of AO dye removal by MF: contact time, adsorbent dose, and initial dye concentration were found to be, respectively, 75 min, 1.2 g, and 5 mg L⁻¹ (experiments were repeated three times). Thus, at these optimum conditions, AO dye removal by MF reach 99%.

3.3.3. Adsorption isotherm

Batch experiments were carried out at a series of initial dye concentrations at the natural pH of the initial solution (pH = 6.4) and at an MF adsorption dose of 1.2 g.

Results (Fig. 17a) show that the adsorption isotherm is of L type according to Sposito classification [39], suggest a good affinity for the solid phase to the adsorbed substance coupled with a decrease in the number of adsorption sites. The adsorbent amount of dye removal at saturation was found to be 6.437 mg g⁻¹.

3.3.4. Modeling

To analyze experimental adsorption data and design an adsorption system, Langmuir and Freundlich models were selected.

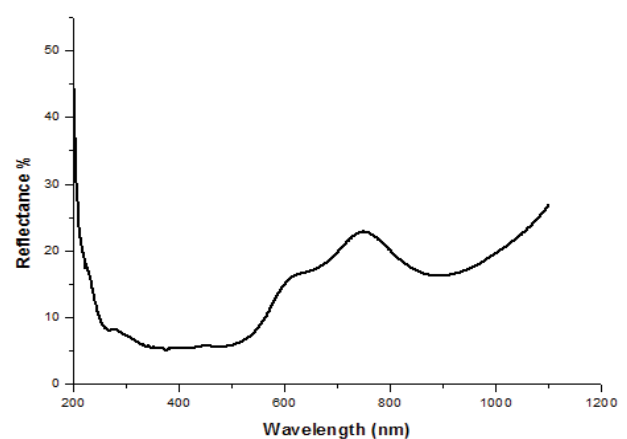


Fig. 15. UV-visible diffuse reflectance spectra (DRS) of MF.

As can be seen from Figs. 17b and c and Table 3 Langmuir model fit well with experimental data ($R^2 = 0.930$) put forward that adsorption process is mainly monolayer. The maximum adsorption capacity deduced from the Langmuir

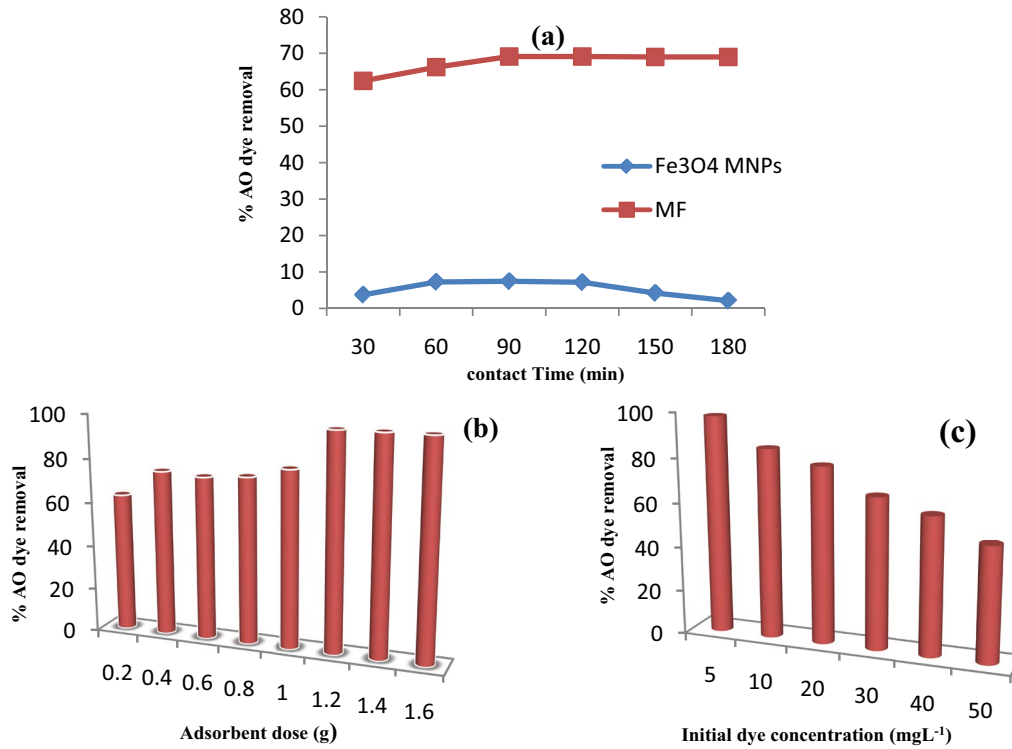


Fig. 16. Effect of experimental parameters on AO dye adsorption. Effect of (a) contact time, (b) adsorbent dose, and (c) initial dye concentration.

Table 3
Isotherm and kinetic parameters for the AO dye adsorption onto MF

| (a) Kinetic parameters | | | | | | |
|---|----------------------------|-------|--|---|-------|-------|
| Pseudo-first-order model | | | Pseudo-second-order model | | | |
| $\ln(q_e - q_t) = \ln q_e - K_1 t$ (4) [40] | | | $\frac{t}{q_t} = \frac{1}{K_2 q_e^2} + \frac{1}{q_e} t$ (5) [41] | | | |
| q_e (mg g ⁻¹) | K_1 (min ⁻¹) | R^2 | q_e (mg g ⁻¹) | K_2 (g mg ⁻¹ min ⁻¹) | R^2 | |
| 0.247 | - | 0.867 | 6.871 | 1.353 | 0.999 | |
| (b) Langmuir and Freundlich parameters | | | | | | |
| Langmuir | | | | Freundlich | | |
| q_{max} (mg g ⁻¹) | K_L | R_L | R^2 | K_F | $1/n$ | R^2 |
| 6.112 | 0.077 | 0.721 | 0.9302 | 1.218 | 0.586 | 0.887 |

q_e : amount of AO adsorbed at equilibrium (mg g⁻¹); q_t : amount of AO adsorbed at time t (mg g⁻¹); K_1 : rate constant of pseudo-first-order (min⁻¹); K_2 : rate constant of pseudo-second-order (g mg⁻¹ min⁻¹); Q_{max} : maximum adsorption capacity (mg g⁻¹); C_e : amount of residual dye at equilibrium (mg L⁻¹); K_L : Langmuir constant (L mg⁻¹); K_F : Freundlich constant; n is an indicator of adsorption effectiveness.

model is 6.11 mg g⁻¹ which confirms very well the experimental quantity.

3.3.5. Kinetic modeling

Pseudo-first and pseudo-second-order models are the most commonly used linear equations to describe kinetics adsorption and determine the adsorption mechanism process. Results show that pseudo-second-order fit well

with experimental data (Fig. 18, Table 3), since the correlation coefficient R^2 is more close to 1 ($R^2 = 0.999$), suggested physisorption process of AO onto MF [41–43].

3.3.6. Comparison with different adsorbents

In order to compare the efficiency of MF adsorbents for AO dye removal to other adsorbents, a list of different adsorbents with their corresponding AO dye removal

percentage was presented in Table 4. It was noticed that the studied natural iron oxide shows an excellent efficiency in adsorbing AO and presents a higher AO dye removal percentage. This natural adsorbent could be comparable to just a few other adsorbents in the reports published previously.

4. Conclusions

In this work, the reverse co-precipitation method to produce Fe_3O_4 nanoparticles (MNPs) is developed in the presence of ferrous and ferric solutions using ammonium hydroxide as a precipitation agent under ultrasound irradiation. TEM analysis shows that the structure of these nanoparticles are spherical with a mesoporous texture. BET-specific surface area was found to be $30.695 \text{ m}^2 \text{ g}^{-1}$.

In addition, natural iron oxide which is a Tunisian iron ore (MF) was characterized and compared to the synthesized oxide. TEM analysis of MF exhibits a rod shape

(nanorods) with a microporous texture. Its specific surface area S_{BET} was determined to be $45.868 \text{ m}^2 \text{ g}^{-1}$.

Optical characterization reveals that synthesized iron oxide exhibited absorption in ultraviolet and visible light regions while the natural iron oxide showed absorption only in the visible light region.

Absorbent properties of these two materials have been studied with respect to an anionic dye, Auramine O, frequently used by textile industries. MF was found to be the better adsorbent with 99% dye removal with specific optimum conditions: 1.2 g of MF, 5 mg L^{-1} of initial dye concentration, and 75 min of contact time. The adsorption process was found to be monolayer and follow pseudo-second-order kinetic model (physisorption).

Regarding their physical, chemical, and optical properties, these two non-toxic materials will be utilized as heterogeneous catalysts in Fenton process for water treatment application, and especially the natural iron oxide due to its

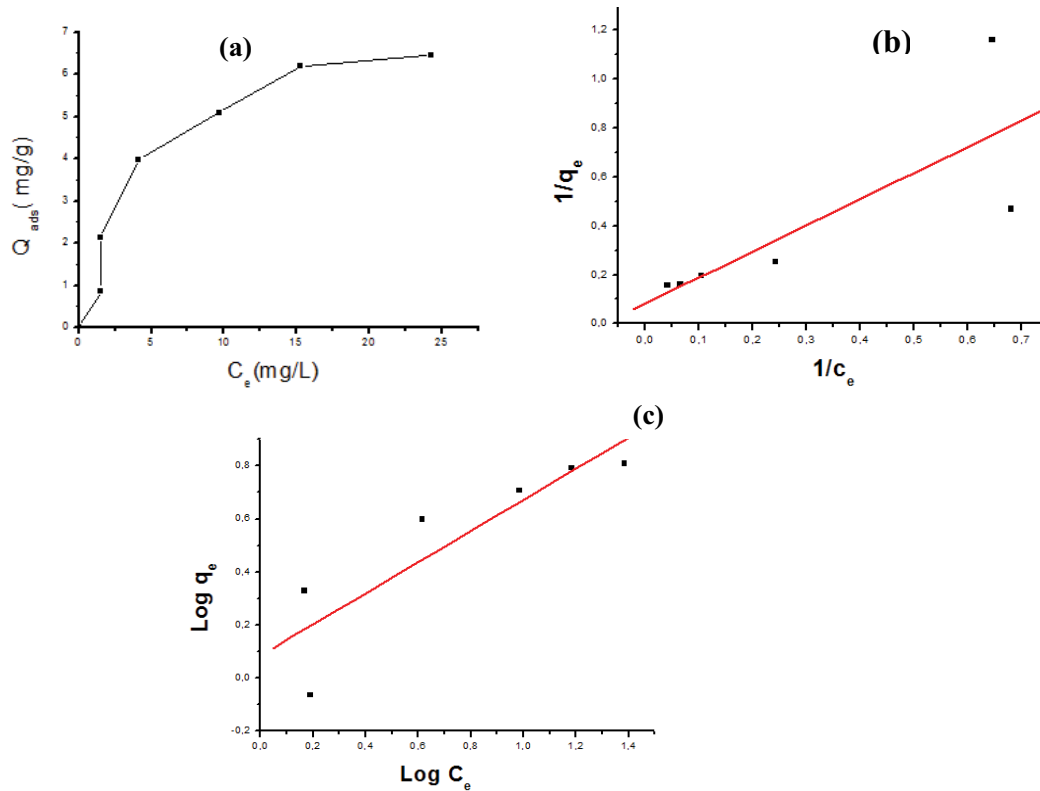


Fig. 17. (a) Adsorption isotherm of AO onto MF adsorbent, (b) Langmuir model, and (c) Freundlich model.

Table 4
Auramine-O dye removal by adsorption on different adsorbents

| Adsorbent | % AO dye removal | References |
|---|------------------|---------------|
| Sodium dodecyl sulfate functionalized magnetite nanoparticles | 74 | [42] |
| Sesame leaf | 89 | [43] |
| Guava leaves | 92 | [44] |
| Natural untreated clay | 95 | [45] |
| Natural iron oxide (MF) | 99 | Present study |

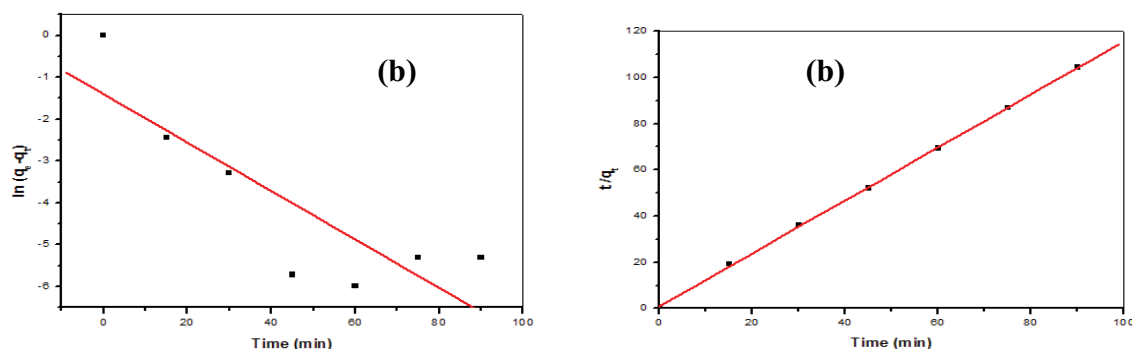


Fig. 18. Kinetic study: (a) pseudo-first-order and (b) pseudo-second-order models.

low cost, abundance, and its efficiency for hazardous dyes treatment such as Auramine O dye.

Acknowledgments

The authors would like to extend their sincere appreciation to King Saud University (Riyadh, Saudi Arabia) for the support of this research through the Researchers Supporting Project number (RSP-2020/147).

References

- [1] V.J. Inglezakis, S.G. Pouloupoulos, Adsorption, Ion Exchange and Catalysis: Design of Operations and Environmental Applications, Elsevier Science, Amsterdam, 2006.
- [2] F.G. Babuna, S. Camur, I.A. Alaton, O. Okay, G. Iskender, The application of ozonation for the detoxification and biodegradability improvement of a textile auxiliary: naphthalene sulphonic acid, *Desalination*, 249 (2009) 682–686.
- [3] H. Zangeneh, A.A.L. Zinatizadeh, M. Feizy, A comparative study on the performance of different advanced oxidation processes (UV/O₃/H₂O₂) treating linear alkyl benzene (LAB) production plant's wastewater, *J. Ind. Eng. Chem.*, 20 (2014) 1453–1461.
- [4] A. Nickheslat, M.M. Amin, H. Izanloo, A. Fatehizadeh, S.M. Mousavi, Phenol photocatalytic degradation by advanced oxidation process under ultraviolet radiation using titanium dioxide, *J. Environ. Public Health*, 2013 (2013) 1–9.
- [5] S.S. Maria, T.B.C. Vanessa, J. Pereira, Drinking water treatment of priority pesticides using low pressure UV photolysis and advanced oxidation processes, *Water Res.*, 44 (2010) 1809–1818.
- [6] B.D. Witte, H.V. Langenhove, K. Demeestere, J. Dewulf, Advanced oxidation of pharmaceuticals: chemical analysis and biological assessment of degradation products, *Crit. Rev. Environ. Sci. Technol.*, 41 (2011) 215–242.
- [7] M. Pérez, F. Torradesa, J.A. García-Hortalb, X.D.J. Peral, Removal of organic contaminants in paper pulp treatment effluents under Fenton and photo-Fenton conditions, *Appl. Catal., B*, 36 (2002) 63–74.
- [8] U. Schwertmann, R.M. Cornell, *The Iron Oxides: Structure, Properties, Reactions, Occurrences and Uses*, 2nd ed., WILEY-VCH, Weinheim, 2003.
- [9] S. Aredes, B. Klein, M. Pawlik, The removal of arsenic from water using natural iron oxide minerals, *J. Cleaner Prod.*, 30 (2012) 208–213.
- [10] F.X. Hu, K.G. Neoh, E.T. Kang, Synthesis and in vitro anti-cancer evaluation of tamoxifen-loaded magnetite/PLLA composite nanoparticles, *Biomaterials*, 27 (2006) 5725–5733.
- [11] K. Nishio, M. Ikeda, N. Gokon, S. Tsubouchi, H. Narimatsu, Y. Mochizuki, S. Sakamoto, A. Sandhu, M. Abe, H. Handa, Preparation of size-controlled (30–100 nm) magnetite nanoparticles for biomedical applications, *J. Magn. Magn. Mater.*, 310 (2007) 2408–2410.
- [12] Z. Ma, H. Liu, Synthesis and surface modification of magnetic particles for application in biotechnology and biomedicine, *J. China Particuol.*, 5 (2007) 1–10.
- [13] J. Bruce, J. Taylor, M. Todd, M.J. Davies, E. Borioni, C. Sangregorio, T. Sen, Synthesis, characterisation and application of silica-magnetite nanocomposites, *J. Magn. Magn. Mater.*, 284 (2004) 145–160.
- [14] C. Alborno, S.E. Jacobo, Preparation of a biocompatible magnetic film from an aqueous ferrofluid, *J. Magn. Magn. Mater.*, 305 (2006) 12–15.
- [15] B.M. Teo, F. Chen, T.A. Hatton, F. Grieser, M. Ashokkumar, Novel one-pot synthesis of magnetite latex nanoparticles by ultrasound irradiation, *Langmuir*, 25 (2009) 2593–2595.
- [16] A.B. Chin, I.I. Yaacob, Synthesis and characterization of magnetic iron oxide nanoparticles via w/o microemulsion and Massart's procedure, *J. Mater. Process. Technol.*, 191 (2007) 235–237.
- [17] E. Teeman, L.N. Brush, N.D. Browning, K.M. Krishnan, Synthesis of phase-pure and monodisperse iron oxide nanoparticles by thermal decomposition Ryan Hufschmid, *Nanoscale*, 7 (2015) 11142–11154.
- [18] W. Zhang, S. Jia, Q. Wu, J. Ran, S. Wu, Y. Liu, Convenient synthesis of anisotropic Fe₃O₄ nanorods by reverse co-precipitation method with magnetic field-assisted, *Mater. Lett.*, 65 (2011) 1973–1975.
- [19] X. Liu, M.D. Kaminski, Y. Guan, H. Chen, H.A. Lui, Preparation and characterization of hydrophobic superparamagnetic magnetite gel, *J. Magn. Magn. Mater.*, 306 (2006) 248–253.
- [20] S. Khelifi, F. Ayari, D.B. Hassan Chehimi, M. Trabelsi-Ayadi, Synthesis and characterization of heterogeneous catalysts and comparison to iron-ore, *J. Chem. Eng. Process. Technol.*, 7 (2016) 1–9, doi: 10.4172/2157-7048.1000316.
- [21] F. Ayari, A. Ben Othmen, S. Khelifi, M. Trabelsi-Ayadi, Photodegradation of Congo red and real textile industries effluent using natural Tunisian iron, *Desal. Water Treat.*, 107 (2018) 316–323.
- [22] S.B. Hammouda, N. Adhoum, L. Monser, Synthesis of magnetic alginate beads based on Fe₃O₄ nanoparticles for the removal of 3-methylindole from aqueous solution using Fenton process, *J. Hazard. Mater.*, 294 (2015) 128–136.
- [23] A. Al-Alawy, E.E. Al-Abodi, R.M. Kadhim, Synthesis and characterization of magnetic iron oxide nanoparticles by co-precipitation method at different conditions, *J. Eng.*, 24 (2018) 60–92.
- [24] N. Wang, L. Zhu, D. Wang, M. Wang, Z. Lin, H. Tang, Sono-assisted preparation of highly-efficient peroxidase-like Fe₃O₄ magnetic nanoparticles for catalytic removal of organic pollutants with H₂O₂/Ultrasound, *Sonochem.*, 17 (2010) 526–533.
- [25] S. Laurent, D. Forge, M. Port, A. Roch, C. Robic, L. Elst, R. Muller, Magnetic iron oxide nanoparticles: synthesis, stabilization, vectorization, physicochemical characterizations and biological applications, *Chem. Rev.*, 108 (2008) 2064–2110.
- [26] Y. Chen, H. Gu, Microwave assisted fast fabrication of Fe₃O₄-MWCNTs nanocomposites and their application as MRI contrast agents, *Mater. Lett.*, 67 (2012) 49–51.

- [27] K. Petcharoen, A. Sirivat, Synthesis and characterization of magnetite nanoparticles via the chemical co-precipitation method, *Mater. Sci. Eng., B*, 177 (2012) 421–427.
- [28] J. Sun, S. Zhou, P. Hou, Y. Yang, J. Weng, X. Li, M. Li, Synthesis and characterization of biocompatible Fe_3O_4 nanoparticles, *J. Biomed. Mater. Res. Part A*, 80 (2007) 333–341.
- [29] M. Srivastava, J. Singh, M. Yashpal, D.K. Gupta, R.K. Mishra, S. Tripathi, A.K. Ojha, Synthesis of superparamagnetic bare Fe_3O_4 nanostructures and core/shell (Fe_3O_4 /alginate) nanocomposites, *Carbohydr. Polym.*, 89 (2012) 821–829.
- [30] M. Ma, Y. Zhang, W. Yu, H. Shen, H.Q. Zhang, N. Gu, Preparation and characterization of magnetic nanoparticles coated by aminosilane, *Colloids Surf., A*, 212 (2003) 219–226.
- [31] A. Manikandan, J.J. Vijaya, J.A. Mary, L.J. Kennedy, A. Dinesh, Structural, optical and magnetic properties of Fe_3O_4 nanoparticles prepared by a facile microwave combustion method, *J. Ind. Eng. Chem.*, 20 (2014) 2077–2085.
- [32] Y. Cao, C. Li, J. Li, Q. Li, J. Yang, Magnetically separable Fe_3O_4 /AgBr hybrid materials: highly efficient photocatalytic activity and good stability, *Nanoscale Res. Lett.*, 10 (2015) 1–6.
- [33] J.S. Markovski, V. Đokić, M. Milosavljević, M. Mitrić, A.A. Perić-Grujić, A.E. Onjia, A.D. Marinković, Ultrasonic assisted arsenate adsorption on solvothermally synthesized calcite modified by goethite, $\alpha\text{-MnO}_2$ and goethite/ $\alpha\text{-MnO}_2$, *Ultrason. Sonochem.*, 21 (2014) 790–801.
- [34] K. Eusterhues, F.E. Wagner, W. Häusler, M. Hanzlik, H. Knicker, K.U. Totsche, I. Kögel Knabner, U. Schwertmann, Characterization of ferrihydrite-soil organic matter coprecipitates by X-ray diffraction and Mossbauer spectroscopy, *Environ. Sci. Technol.*, 42 (2008) 7891–7897.
- [35] L.C. Oliveira, T.C. Ramalho, E.F. Souza, M. Gonçalves, D.Q. Oliveira, M.C. Pereira, J.D. Fabris, Catalytic properties of goethite prepared in the presence of Nb on oxidation reactions in water: computational and experimental studies, *Appl. Catal., B*, 83 (2008) 169–176.
- [36] N. Sankararamkrishnan, A. Gupta, S.B. Viduarthi, Enhanced arsenic removal at neutral pH using functionalized multiwalled carbon nanotubes, *J. Environ. Chem. Eng.*, 2 (2014) 802–810.
- [37] J. Cai, S. Chen, M. Ji, J. Hu, Y. Ma, L. Qi, Organic additive-free synthesis of mesocrystalline hematite nanoplates via two dimensional oriented attachment, *CrystEngComm*, 8 (2014) 1553–1559.
- [38] A. Aiswal, S. Banerjee, R. Mani, M.C. Chattopadhyaya, Synthesis, characterization and application of goethite mineral as an adsorbent, *J. Environ. Chem. Eng.*, 1 (2013) 281–289.
- [39] G. Sposito, Surface reaction in natural colloidal system, *Chimia*, 43 (1989) 169–176.
- [40] Y.S. Ho, G. McKay, Kinetic models for the sorption of dye from aqueous solution by wood, *Process Saf. Environ. Prot.*, 76 (1998) 183–191.
- [41] Y.S. Ho, G. McKay, Pseudo-second order model for sorption processes, *Process Biochem.*, 34 (1999) 451–465.
- [42] C. Muthukumar, V.M. Sivakumar, S. Sumathi, M. Thirumarimurugan, Adsorptive removal of recalcitrant Auramine-O dye by sodium dodecyl sulphate functionalized magnetite nanoparticles: isotherm, kinetics and fixed bed column studies, *Int. J. Nanosci.*, 19 (2020) 1793–5350.
- [43] L.E. Liu, F. Yu, J. Liu, X. Han, H. Zhang, B. Zhang, Removal of Auramine O from aqueous solution using sesame leaf: adsorption isotherm and kinetic studies, *Chem. Asian J.*, 25 (2013) 1991–1998.
- [44] R.W. Gaikwad, S.A.M. Kinldy, Studies on auramine dye adsorption on *Psidium* guava leaves, *Korean J. Chem. Eng.*, 26 (2009) 102–107.
- [45] A. Ozturk, E. Malkoc, Adsorptive potential of cationic basic yellow 2 (BY2) dye onto natural untreated clay (NUC) from aqueous phase: mass transfer analysis, kinetic and equilibrium profile, *Appl. Surf. Sci.*, 229 (2014) 105–115.